Temperature-Dependent Interplay between Structural and Charge Carrier Dynamics in CsMAFA-Based Perovskites

Jiashang Zhao, Xiaohui Liu, Zijin Wu, Bahiya Ibrahim, Jos Thieme, Geert Brocks, Shuxia Tao, Lars J. Bannenberg, and Tom J. Savenije*

State-of-the-art triple cation, mixed halide perovskites are extensively studied in perovskite solar cells, showing very promising performance and stability. However, an in-depth fundamental understanding of how the phase behavior in $Cs_{0.05}FA_{0.85}MA_{0.10}Pb(I_{0.97}Br_{0.03})_3$ (CsMAFA) affects the optoelectronic properties is still lacking. The refined unit cell parameters a and c in combination with the thermal expansion coefficients derived from X-ray diffraction patterns reveal that CsMAFA undergoes an α–β phase transition at $\approx$280 K and another transition to the γ-phase at $\approx$180 K. From the analyses of the electrodeless microwave photoconductivity measurements it is shown that shallow traps only in the γ-phase negatively affect the charge carrier dynamics. Most importantly, CsMAFA exhibits the lowest amount of microstrain in the β-phase at around 240 K, corresponding to the lowest amount of trap density, which translates into the longest charge carrier diffusion length for electrons and holes. Below 200 K a considerable increase in deep trap states is found most likely related to the temperature-induced compressive microstrain leading to a huge imbalance in charge carrier diffusion lengths between electrons and holes. This work provides valuable insight into how temperature-dependent changes in structure affect the charge carrier dynamics in FA-rich perovskites.

1. Introduction

Over the last decade metal halide perovskites (MHPs) have attracted a tremendous amount of attention owing to their favorable intrinsic optoelectronic properties, such as high absorption coefficients ($\approx$10⁵ cm⁻¹), fairly balanced effective carrier mobilities (tens of cm² V⁻¹ s⁻¹), remarkable defect tolerance (10¹³–10¹⁶ cm⁻³), as well as ease of fabrication.[1–5] Hence, a variety of applications ranging from thin-film photovoltaics to light-emitting devices have been developed.[5–7] Recently, the rapid progress in the development of single-junction perovskite solar cells (PSCs) achieved a certified power conversion efficiency (PCE) of 26.1%.[8] These high PCEs are generally found in FA-rich MHPs combined with a small amount of Cs and/or MA.[9–16] Previous work has shown that the improved phase stability of FA-rich MHPs is achieved by manipulating the Goldschmidt tolerance factor by mixing MA, Cs, and Br.[17] Beyond terrestrial applications, PSCs are promising candidates for space applications due to their unique features such as their superior radiation resistance.[18] Recent work on complete solar cells at low temperatures[19,20] has shown that the performance of $Cs_{0.05}MA_{0.10}FA_{0.85}Pb(I_{0.97}Br_{0.03})_3$ (CsMAFA)-based PSCs increased by 8% at 220 K in comparison to room temperature due to the improved open-circuit voltage, which was linked to the elimination of intrinsic defects present at that temperature.[19] Another study on the temperature-dependent performance of a $(Cs_{0.05}FA_{0.79}MA_{0.16}Pb(I_{0.83}Br_{0.17})_3)$

J. Zhao, X. Liu, B. Ibrahim, J. Thieme, T. J. Savenije
Department of Chemical Engineering
Faculty of Applied Sciences
Delft University of Technology
Delft HZ 2629, The Netherlands
E-mail: T.j.Savenije@tudelft.nl

Z. Wu, G. Brocks, S. Tao
Materials Simulation and Modelling
Department of Applied Physics
Eindhoven University of Technology
Eindhoven MB 5600, The Netherlands

L. J. Bannenberg
Department of Radiation Science and Technology
Faculty of Applied Sciences
Delft University of Technology
Delft JB 2629, The Netherlands

G. Brocks
Computational Chemical Physics
Faculty of Science and Technology and MESA+ Institute for Nanotechnology
University of Twente
P. O. Box 217, Enschede AE 7500, The Netherlands

**ADVANCED
SCIENCE NEWS**

www.advancedsciencenews.com

**ADVANCED
FUNCTIONAL
MATERIALS**

www.afm-journal.de

device revealed that inhibition of carrier extraction across interfaces leads to severe performance losses at $T < 200$ K.[20] Despite these insights there is little knowledge how the optoelectronic properties of FA-rich MHPs are affected by temperature. Therefore, it is of great interest to investigate the fundamental optoelectronic properties of these intrinsic absorber layers with temperature in an effort to explain the superior properties of this class of materials and eventually to come to compositions with even improved potentials.

In general, cooling MHPs in the range between 300–100 K is accompanied by one or more structural phase transitions.[21] The change of the crystal structure largely influences the photoluminescence (PL) and charge carrier recombination processes in $(FAPbI_3)_{0.85}(MAPbBr_3)_{0.15}$ layers.[22] However, the underlying relationship between their structural and optoelectronic properties is not fully understood and there are still several open questions to be further resolved. For instance, how does temperature-induced lattice microstrain play a role in the formation of defect states and how do these defects affect the charge carrier recombination dynamics? Furthermore, shallow defects are generally considered to be not detrimental to the PCE since they are close to the edges of the bands.[23] It is unclear how these shallow defects affect the dynamics upon cooling. Besides, there is typically a mismatch in thermal expansion coefficients between the MHP layer and substrate affecting the phase behavior and optoelectronic properties. In addition, excess PbI_2 has been widely used in MHPs as a passivation strategy to improve the performance of PSCs and its impact on the structure and recombination kinetics as well as stability has also been extensively investigated.[24–29] However, systematic studies on the role of excess PbI_2 on the low-temperature structural and optoelectronic properties of FA-rich MHPs are still missing. For these reasons it is important to investigate how the temperature affects the structure and consecutively the optoelectronic properties and stability in CsMAFA-based MHPs.

In this work, we studied the relationship between structural and optoelectronic properties of CsMAFA layers as a function of temperature by means of X-ray diffraction (XRD), absorption and PL, as well as contactless photoconductivity measurements. This paper starts with the temperature-dependent XRD analysis of CsMAFA with a small excess of PbI_2. The XRD patterns are all refined revealing an α–β phase transition between 298 and 270 K, and a further phase transition to the γ-phase at around 180 K. We continue with optical measurements, which show that the band gap monotonically reduces without discontinuities from 298 to 100 K. Then time-resolved microwave photoconductivity measurements over the same temperature range are carried out using a short laser pulse at an excitation wavelength of 600 nm. By recording multiple traces with various intensities at each temperature, the effect of the intensity on the decay kinetics is studied in detail. These traces are fitted using a kinetic model including shallow and deep states in the band structure.

From the fits, we conclude that first, upon cooling, the mobility is enhanced in the β-phase due to reduced phonon scattering. Upon further cooling, the mobility decreases again in the γ-phase because of a substantial increase in deep traps, rather than a change in the effective mass of electrons and holes, as shown by density functional theory calculations. Furthermore, shallow states affect the charge carrier dynamics negatively due to the re-

duced thermal energy upon cooling. Moreover, on entering the γ-phase, the deep trap density increases at least one order of magnitude compared with the density at 200 K. This is most likely related to the increase in microstrain in the γ-phase. Finally, we find that excess PbI_2 inhibits phase retention in CsMAFA layers by reducing the mismatch of the thermal expansion coefficient between the quartz and perovskite. Most importantly, CsMAFA exhibits the lowest deep trap density at 200 K in the β-phase, consistent with the highest PCE in FA-rich based PSC at 220 K.[19] This is in line with the fairly balanced electron and hole charge carrier diffusion lengths, which we calculated using the kinetic constants found at 200 K.

2. Results and Discussion

CsMAFA layers (of about 500 nm thickness) were deposited on quartz substrates by spin-coating followed by the introduction of the antisolvent to accelerate the nucleation and growth of the perovskite layer.[32,33] A 5% excess PbI_2 was used in the precursor solution to improve the structural properties (see Experimental Section for more detailed information). In Figure S1a (Supporting Information) the optical attenuation spectrum of CsMAFA is provided, showing optical absorption onset at around 800 nm (1.55 eV) in line with the literature.[34,35] Figure S1b (Supporting Information) presents the XRD pattern confirming that the layer indeed shows excess PbI_2 by the diffraction peaks located at $2\theta = 12.7°$, $25.4°$, and $38.1°$. Figure S1c (Supporting Information) shows the top view SEM image of CsMAFA displaying the compact and polycrystalline nature of the perovskites.

In order to identify where the excess PbI_2 is located in the CsMAFA sample, we carried out grazing-incidence XRD (GIXRD) measurements with incident angles ranging from $\omega = 0.2°$ to $5°$, as shown in **Figure 1a**. Using this approach, we are able to investigate the nature of the layer at various depths, since the larger the incident angle, the deeper the layer is probed. The ratios of the PbI_2 peak at $2\theta = 12.7°$ and the perovskite (100) peak at $2\theta = 14°$ are collected in Table S1 (Supporting Information) for the different incident angles. Initially, the ratio reduces with increasing the angle from $\omega = 0.2°$ to $1°$, which may be partly caused by the strong preferred orientation of the PbI_2. Since only the (002) peak of PbI_2 is observed (Figure S1b, Supporting Information) and the fact that changing the incident angle changes the direction of the Q-vector/probed lattice vector, a decrease of the PbI_2 reflection at $2\theta = 12.7°$ with increasing ω is also expected. Most importantly, the ratio increases significantly from $3°$ to $5°$ implying that the excess PbI_2 is most likely residing at the bottom part of the layer instead of the bulk.

To study how the structure of the CsMAFA layer changes with temperature, XRD was performed between 298 and 100 K. Figure 1b shows an overview of the XRD patterns with the peak at 12.7°, indicated by the vertical dashed line, confirming the presence of excess PbI_2 in the CsMAFA sample. All peaks at 298 K correspond to the cubic (α)-phase of the perovskite indicated by the pattern at the bottom of Figure 1b (See also Figure 1a for corresponding planes).[36,37] At 270 K, a new peak at 22.2° starts to appear and becomes more pronounced on cooling, marked by the blue shade. This is attributed to the phase transition from the α- to the tetragonal (β)-phase between 298 and 270 K, consistent with the α–β phase transition at 285 K reported in pure

**ADVANCED
SCIENCE NEWS**

www.advancedsciencenews.com

**ADVANCED
FUNCTIONAL
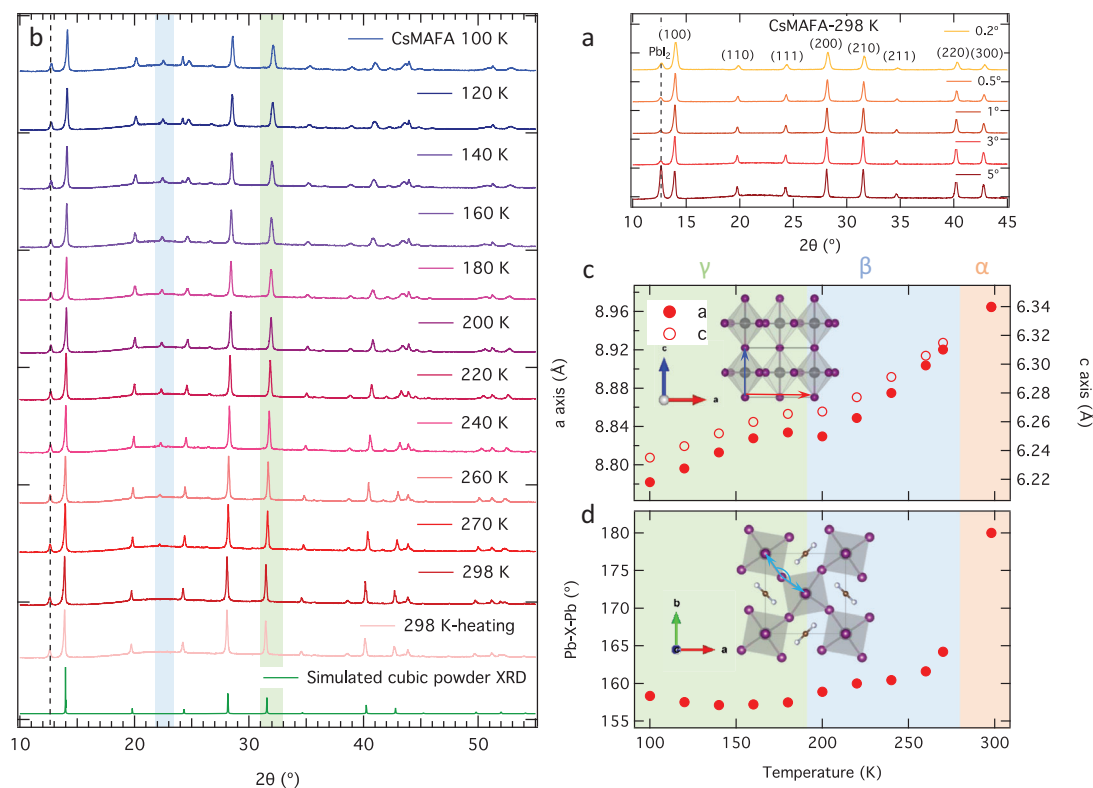MATERIALS**

www.afm-journal.de

Figure 1. a) Normalized grazing-incidence XRD patterns with incident angles ranging from 0.2° to 5° for the CsMAFA layer at 298 K. b) Temperature dependence of an overview of the Bragg–Brentano XRD patterns (Cu Kα X-radiation) of the CsMAFA layer deposited on quartz. c) Lattice parameters a (left axis, indicated by the red arrow) and c (right axis, indicated by the blue arrow). d) Pb—X—Pb bond angles (indicated by light blue arrows) extracted from the refinement of XRD as a function of temperature.

FAPbI$_3$.[38] Furthermore, at 180 K, an obvious peak broadening at $\approx$32° and 41° is observed (green shade), implying a second phase transition to a tetragonal γ-phase (retaining P4/mbm, #127) in agreement with the β–γ phase transition reported for FAPbI$_3$.[37,38] It is worth noting here that the phase transition temperature can be slightly shifted for the FA-rich mixed cation and mixed halide perovskites in comparison to pure FAPbI$_3$.[39] On lowering the temperature down to 140 K, additional peak splitting leads to a narrow and broad peak at $\approx$24°, indicative of a small amount of additional phase consistent with the (111) peak of the α-phase. Importantly, when the layer is heated up to 298 K, a fully reversible conversion to the original cubic phase is observed and no phase segregation occurs.

To better understand and quantify how the crystal structure varies, we refined the XRD patterns at each temperature and were able to extract the unit cell parameters as well as the corresponding Pb—X—Pb bond angle using the space group P4/mbm no.127 (See Figure S2, Supporting Information, for the refinement of XRD). We should note here that the refinement of thin film-based XRD data is somewhat limited as compared to the refinement of XRD data recorded on powders. Nevertheless, since we intend to link the optical and conductivity properties to the structure in the thin film, we focused in this work on layers and did not measure any powder samples. In addition, due to the polycrystalline nature and weak preferential orientation of the CsMAFA layer, the XRD patterns show for example at room temperature

all diffraction peaks expected for cubic powder XRD as shown at the bottom of Figure 1b, making the refinement still feasible and reliable.

Figure 1c,d shows the lattice parameters a, c and the Pb—X—Pb bond angle in the ab plane, respectively, as a function of temperature (see Figure S3, Supporting Information, for the evolution of the ratio $a/\sqrt{2}c$ with temperature). In Figure 1c, the sizes of the a- and c-axes continuously decrease due to lattice contraction upon cooling.[38,40] At $\approx$180 K, an inflection point in both directions corresponds to the phase transition from the β- to γ-phase.[22,37,38] The discontinuity at $\approx$180 K in the a-direction is slightly larger compared to the c-direction, indicating that the titling of PbI$_6$ octahedra is more severe in the ab plane than the distortion along the c-direction. Figure 1d shows that the Pb—X—Pb bond angle abruptly reduces from 180° to 165° corresponding from the α- to β-phase,[37] implying that the crystal structure is more distorted in the ab plane than in the c-direction in the β-phase. In addition, the unit cell volume versus temperature is given in Figure S4 (Supporting Information). The volumetric thermal expansion coefficients, α_v, in the β- and γ-phases are $422 \pm 20 \times 10^{-6}$ K^{-1} and $214 \pm 15 \times 10^{-6}$ K^{-1}, respectively, which are in agreement with previously reported values for FAPbI$_3$.[37]

Distortion of the ideal crystal structure, by either expansion or contraction of the unit cell, leads to an increase of the lattice strain in perovskites. A common lattice strain in polycrystalline films is microstrain (ϵ), which can be evaluated by peak broadening.

ADVANCED
SCIENCE NEWS

www.advancedsciencenews.com

ADVANCED
FUNCTIONAL
MATERIALS
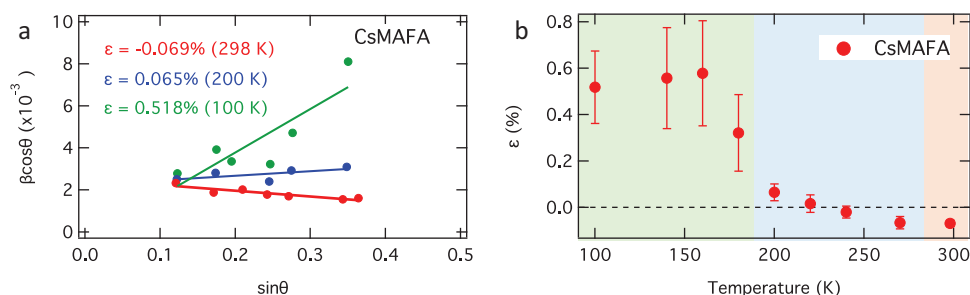
www.afm-journal.de

Figure 2. a) Williamson–Hall plot of the CsMAFA layer at three phases. b) Evolution of microstrain (ϵ) with the temperature ranging from 298 to 100 K.

The relationship between the peak width (β) and microstrain can be represented by the Williamson–Hall plot (W–H plot) method (See Note S1, Supporting Information, in more detail).[41,42] To quantitatively reveal how temperature affects the microstrain in the CsMAFA layer, we analyzed the microstrain evolution during cooling using the W–H plot. **Figure 2a** shows the plot of $\beta\cos\theta$ as a function of $\sin\theta$, from which the microstrain can be deduced from the slope. It is worth noting that a negative slope indicates a tensile strain, while a positive slope originates from a compressive strain. Interestingly, a small tensile strain is observed in the CsMAFA layer at 298 K. It is most likely due to the cooling process after annealing during the fabrication of the CsMAFA layers. In Figure 2b, as temperature decreases, the tensile strain reduces to 0 and eventually becomes compressive, reaching maximum values in the γ-phase. Therefore, the smallest microstrain is observed at around 220 K. Moreover, we should note that the fit becomes worse below 200 K, as shown by the large error bars in Figure 2b. These relatively large errors in the γ-phase indicate the presence of anisotropic microstrain.

Next, to gain more insight into the optical properties of CsMAFA, temperature-dependent absorption, and PL spectra were recorded in the range from 293 to 100 K, as shown in **Figure 3a** (See Figures S5 and S6, Supporting Information, for more temperatures). It can be observed that as temperature decreases, the onset of the absorption gradually shifts to higher wavelengths, corresponding to a similar redshift of the PL emission maximum. The absorption and PL spectra recorded upon heating overlap with the spectra recorded upon cooling, as given by the dashed lines, indicating that the evolution of the optical properties with temperature is fully reversible and changes in the spectra are not caused by the decomposition or degradation of the samples.
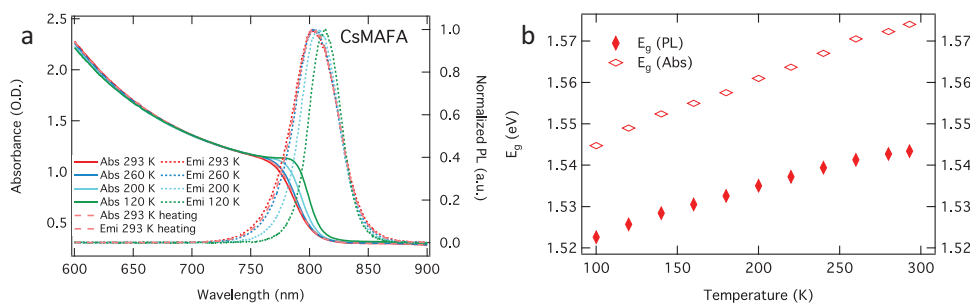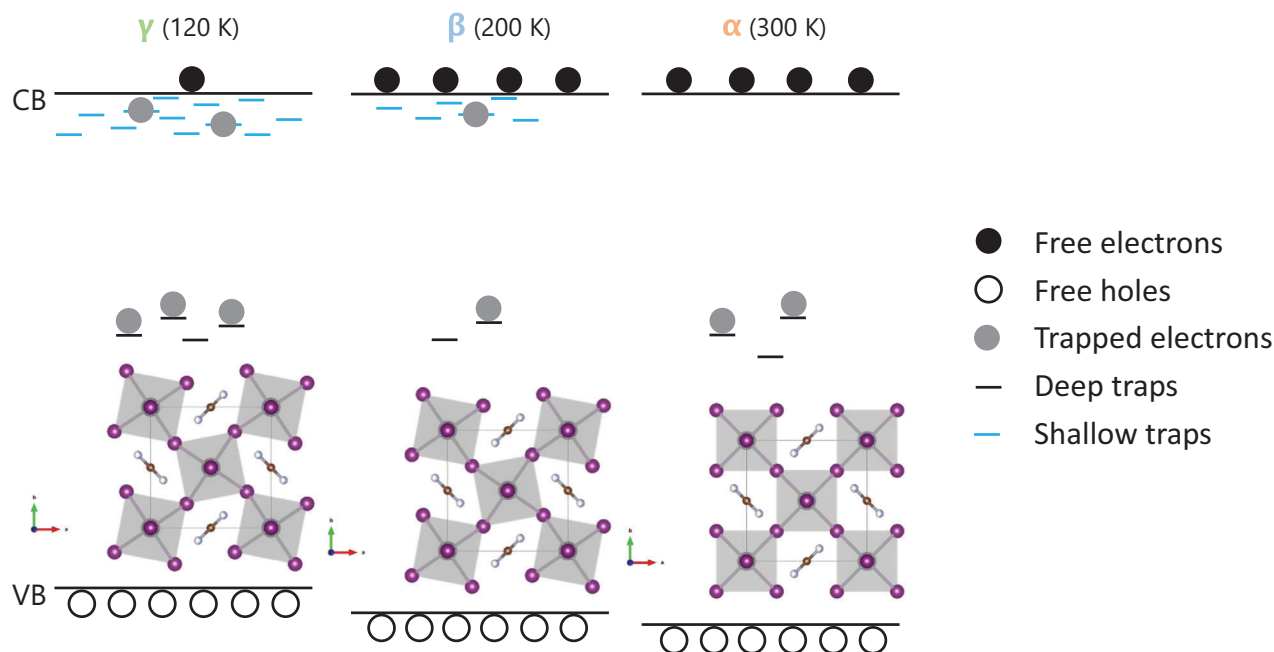
In Figure 3b, we plot the optical band gap (E_g Abs) and the maximum PL emission (E_g PL) as a function of temperature. Based on the reported binding energies of FA-rich perovskites,[44,54–57] we expect that the contribution of excitons to the absorption and PL spectra is limited in the studied temperature range. This is substantiated by our calculations on the ratio between free charges and excitons using the Saha equation (See Equation (S2), Supporting Information). On decreasing the temperature, E_g monotonically reduces without discontinuities comparable to other FA-rich perovskites.[43,44] This implies that neither the tilting of the inorganic octahedra nor the rotational degree of freedom of the organic cation changes abruptly. Otherwise, these structural changes would lead to an abrupt energetic shift like in MAPbI$_3$ for the transition from the β- to γ-phase.[21,45] The continuous reduction in E_g upon cooling in CsMAFA is similar to that of other perovskites, in contrast to general semiconductors.[46,47] This is commonly attributed to the fact that as the lattice shrinks, the Pb-s and I-s orbitals overlap increases, leading to a rise of both the valence band maximum (VBM) and the conduction band minimum (CBM). Since the band edge shift of the VBM is larger than that of the CBM,[48,49] E_g becomes smaller as temperature decreases, as illustrated in **Scheme 2**.

To investigate the optoelectronic properties of the CsMAFA layer upon cooling, we conducted temperature-dependent time-resolved microwave conductivity (TRMC) measurements from 298 K down to 120 K on pulsed excitation at $\lambda = 600$ nm. A photo and explanation describing the adapted microwave cell enabling it to vary temperature are provided in Note S3 (Supporting Information). **Figure 4a–d** shows the photoconductance traces (ΔG) normalized by the number of absorbed photons as a function of time at 298, 260, 200, and 120 K. The initial increase of the signal

Figure 3. a) Temperature dependence of the absorption (solid line, left axis) and normalized photoluminescence spectra (dotted line, right axis) of the CsMAFA layer excited with violet LED light ($\lambda = 405$ nm). Dashed lines indicate the data recorded upon heating. b) Evolution of bandgap energy (E_g) extracted from PL and absorption as a function of temperature for the CsMAFA layer.

**ADVANCED
SCIENCE NEWS**

www.advancedsciencenews.com

**ADVANCED
FUNCTIONAL
MATERIALS**

www.afm-journal.de

Scheme 2. An illustration of the proposed energy band diagram at different phases. The crystal structures are visualized by VESTA[61] (see the inset of Figure 1c for a side view of the crystal structure).

originates from the generation of free charge carriers, while the decay is attributed to the immobilization of excess charge carriers via trapping or the recombination of electrons and holes. At low intensities, the decay kinetics is predominantly determined by non-radiative, first-order recombination mediated via deep trap states. With increasing laser pulse intensities, the decay kinetics become faster, which is due to enhanced second-order electron–hole recombination. This type of behavior has been observed and described previously for MHPs.[50–53]

The maximum signal height represents the product of the free charge carrier generation yield, φ, and the sum of the electron and hole mobility, $\Sigma\mu$ (See Equation (4) in the Experimental Section). Given the low exciton binding energy of 10–24 meV reported for FA-rich MHPs in different phases,[44,54–57] the majority of the excitons will dissociate into free charges, and the free charge carrier generation yield, φ, will be close to unity in both α- and β-phases (Figure S7, Supporting Information). Hence on comparing Figure 4a,b, corresponding to the conversion from the α- to the β-phase, the rise in signal size can be attributed to the increase of $\Sigma\mu$ in the β-phase.

On reducing the temperature to 120 K corresponding to the γ-phase, three important observations can be noticed: first, the maximum TRMC signal significantly reduces (Figure 4d). It is worth noting here that even at 120 K we can still assume that φ is close to unity considering the relatively low carrier densities (See calculations in Figure S7, Supporting Information, using the Saha equation[58]). Most importantly, the carrier lifetimes become evidently longer with decay times extending up to hundreds of microseconds (Figure S8, Supporting Information). Finally, the charge carrier decay dynamics exhibit a completely different intensity dependence than in the α- and β-phases, with most of the TRMC traces overlapping at low incident light intensities. These observations suggest a substantial increase in trap states. Note,

that the charge carrier dynamics are fully reversible when the CsMAFA layer is heated up back to 298 K (Figure S9, Supporting Information), implying that all phenomena observed at low temperatures are related to the phase transitions and changes in thermal energy.

Basically, the mobility of electrons and holes is determined by their effective masses and scattering time. To understand the origin of the increase in $\Sigma\mu$, density functional theory (DFT) calculations were carried out to obtain the effective mass of electrons (m_e) and holes (m_h) at different phases. As input, we used the crystal structures and lattice parameters obtained from the refinement of the XRD patterns, as shown in Figure S10 (Supporting Information) (See Note S2, Supporting Information, for detailed information). The calculation of m_e and m_h was performed in two different directions/paths from Z to A and from Z to Γ in the Brillouin zone (Figure S11, Supporting Information). From Figure S12 (Supporting Information) it is clear that m_e and m_h remain fairly constant with small fluctuations across a temperature range from 298 to 100 K, regardless of the phases, in line with previous reports.[54] Hence, we can conclude that the enhancement of $\Sigma\mu$ in the β-phase is not due to the change in effective mass of the electrons or holes. The increased mobility is most likely a result of the reduced phonon scattering with decreasing temperature, in good agreement with previous findings in FA-rich MHPs.[55] Moreover, we can also rule out that the reduction in the TRMC signal observed at 120 K is attributed to a change in effective mass of both carriers. Instead, this reduction is most likely due to the substantial increase in deep and shallow traps. In addition, the calculation also demonstrates that m_e and m_h are fairly comparable, with a ratio close to 1:1 irrespective of the perovskite phases. Therefore, the lowering of the TRMC signal at 120 K is likely connected to the formation of a substantial increase in trap states for one of the carriers.
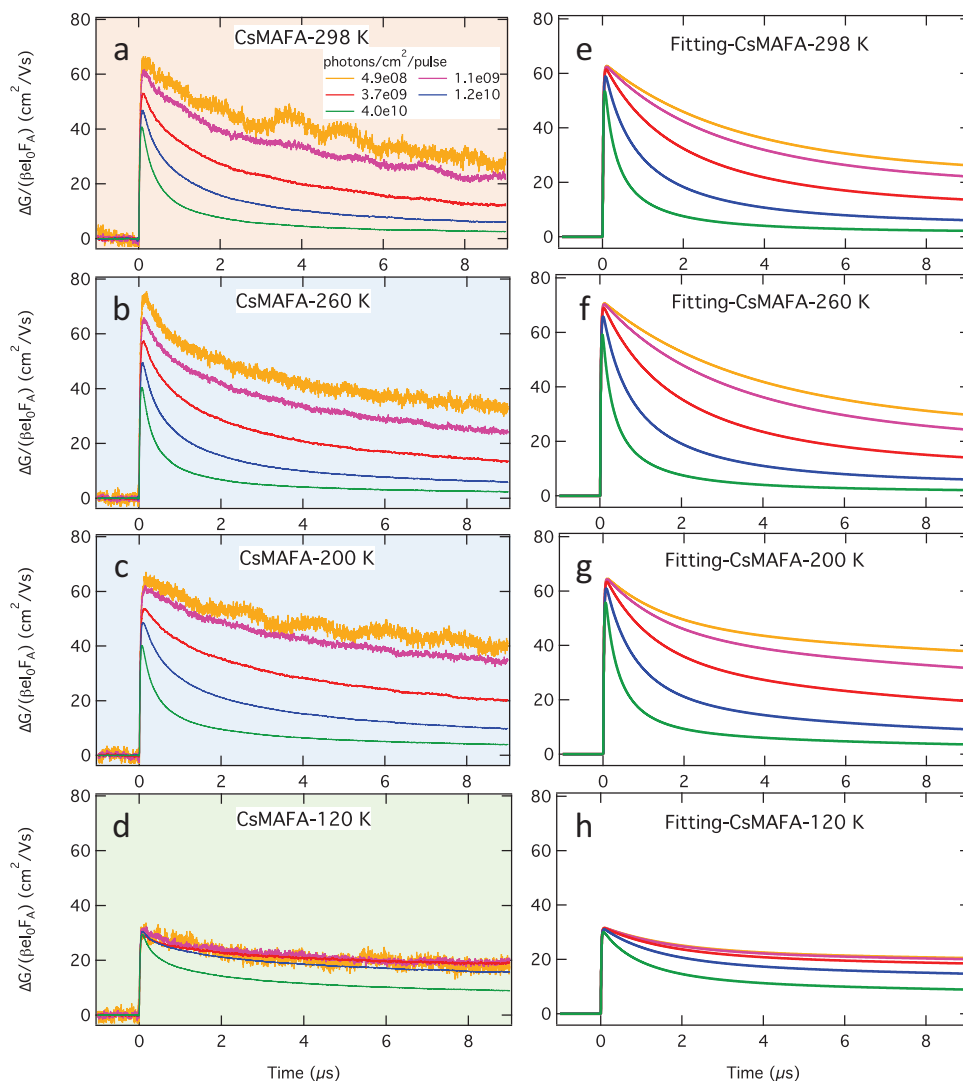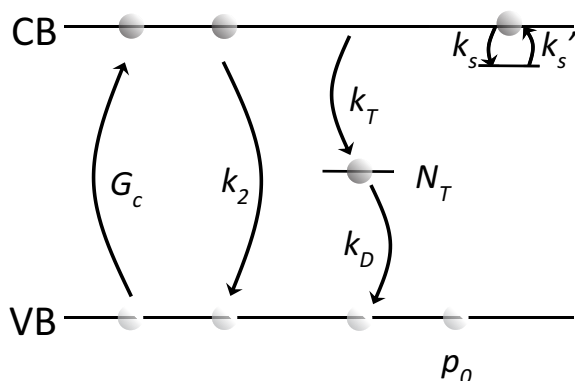
**ADVANCED
SCIENCE NEWS**

www.advancedsciencenews.com

**ADVANCED
FUNCTIONAL
MATERIALS**

www.afm-journal.de

Figure 4. a–h) Experimental photoconductance traces (left panels) and corresponding fitting (right panels) for the CsMAFA sample at 298 (a,e), 260 (b,f), 200 (c,g), and 120 K (d,h) recorded on excitation at 600 nm with incident light intensities ranging from 10^8–10^{10} photons cm^{-2} per pulse.

To verify our above hypothesis, we modeled the photoconductance traces using an adapted kinetic model including shallow states (See **Scheme 1**), previously successfully used to describe the photophysical processes in $(FA_{0.79}MA_{0.15}Cs_{0.06})Pb(I_{1-x}Br_x)_3$ (See Note S3, Supporting Information, for a used set of differential Equations (S5)–(S8), Supporting Information).[51] The detailed global, iterative fitting procedure is summarized in Note S3 (Supporting Information). Important to note here is that a shallow state is defined as a state from which a charge can thermally escape back to the CB. In contrast, a deep electron defect only recombines with a corresponding hole in the VB. Since the optical absorption measurements indicate that the absorption coefficient does not vary a lot with temperature and the fact that the absorption and band-to-band recombination are basically coupled processes,[59] we tried to keep the second-order recombination constant during the fitting procedure.[60] Furthermore, we kept the ratio between electron and hole mobility constant at 1, since the ratio of m_e and m_h remains similar with temperature. The

fits are shown in Figure 4e–h, matching the experimental traces well (See Figure S13, Supporting Information, for other temperatures in log–lin representations). All kinetic parameters are collected in **Table 1**. First of all, the $\Sigma\mu$ in the α-phase amounts to 64 cm^2 V^{-1} s^{-1} and increases to 72 cm^2 V^{-1} s^{-1} at 260 K in the β-phase. Although all other parameters remain fairly constant, the concentration of deep traps (N_T) reduces to 1×10^{13} cm^{-3} at 200 K. This seems to be consistent with the previously reported device efficiencies peaking at 220 K.[19] Moreover, below 240 K, shallow trap states start to play a role in the carrier recombination processes with comparable values between trapping (k_s) and de-trapping rate (k_s'). When entering the γ-phase, in addition to the shallow traps, the number of deep traps, N_T increases and is at least one order of magnitude higher than at 200 K. Furthermore, the ratio of k_s/k_s' increases to 4, implying that the electrons are most of the time residing in shallow states. These observations are all in line with the band diagram depicted in Scheme 2 for the different phases of CsFAMA.

2311727 (6 of 13)

**ADVANCED
SCIENCE NEWS**

www.advancedsciencenews.com

**ADVANCED
FUNCTIONAL
MATERIALS**

www.afm-journal.de

Scheme 1. Kinetic model of charge carrier processes initiated by photoexcitation of CsMAFA. G_c represents the photo generation of charge carriers; k_2 depicts the second-order recombination rate. Electron trap-mediated recombination is described by a trapping rate, k_T, and a depopulation rate, k_D. The two small opposite arrows indicate the immobilization of electrons in shallow trap states with trapping rate k_s and thermal release rate k_s'.

Knowing all these rate constants enables us to calculate the charge carrier diffusion lengths (Λ) for electrons and holes (see **Figure** 5a) at low carrier densities, where defect trapping plays an important role. These values are calculated by determining the half-lifetimes of electrons and holes and multiplying them by their respective mobility. Above 200 K we observe high values of Λ ≈15 and 80 µm for electrons and holes, respectively. Below 200 K the Λ values for holes halve but for electrons, the reduction in Λ is more severe yielding values less than 1 µm. This large asymmetry in Λ could lead to space charge-limited current, heavily reducing the power conversion efficiency of the corresponding cell. Above 200 K, Λ values for electrons and holes are adequately high and relatively balanced with a small maximum at around 240 K. Apart from the diffusion length, the resulting concentrations of mobile electrons and holes generated under AM 1.5 steady-state illumination are important for the resulting Fermi level splitting, which determines the eventual voltage of a corresponding solar cell. In Figure 5b the resulting carrier concentrations are provided as a function of temperature. Since the Fermi level splitting is defined by

$$\mu_F = \frac{kT}{q} \, ln \frac{(n_0 + \Delta n)\,(p_0 + \Delta p)}{n_i^2} \tag{1}$$

where the $\frac{kT}{q}$ is the thermal energy, n_i is the intrinsic carrier concentration, n_0 and p_0 are thermal-equilibrium concentrations of electrons and holes, and Δn and Δp are the concentrations of photogenerated excess electrons and holes, respectively. Since the product of excess electrons and holes ($\Delta n \Delta p$) remains more or less constant as a function of temperature we deduce that the voltage is not heavily affected by the defects formed in the γ-phase.

To investigate how excess PbI_2 affects the structural and optoelectronic properties in FA-rich MHPs, we prepared CsMAFA samples with a stoichiometric ratio, denoted as CsMAFA-st, and performed the same set of measurements, so without the excess PbI_2. First, from the top view SEM images (Figure S14a,b, Supporting Information), the average crystal domain size of CsMAFA (≈200 nm) is almost twice as large as that of the CsMAFA-st (≈100 nm), as demonstrated in the insets, in good agreement with XRD patterns showing that CsMAFA reveals narrower diffraction peaks in comparison to the CsMAFA-st (Figure S14d, Supporting Information). Second, XRD measurements as a function of temperature were performed, but we did not apply data refinement and microstrain calculations to CsMAFA-st, which will be discussed later on. To picture what happens in this layer, similar optical and TRMC measurements were carried out (See Figures S16 and S17, Supporting Information). The absorption spectra for the two layers are comparable, but the PL intensity of CsMAFA is almost a factor of 2 higher as compared to that of CsMAFA-st at 298 K (Figure S16b, Supporting Information). This can be explained by that defects at the grain boundaries are suppressed due to the increased crystal domain size in CsMAFA. Regarding the TRMC measurements at room temperature, the signal height for CsMAFA-st is almost a factor 2 lower in comparison to the CsMAFA. We attribute this reduction to the lower effective mobility that is related to the smaller crystal domain size of CsMAFA-st,[62] confirmed by our SEM measurements (Figure S14a,b, Supporting Information). Previously, similar effects on $MAPbI_3$ and other compositions with excess PbI_2 have been reported.[29,63–65]

Next, we investigated the photoconductivity of CsMAFA-st at various temperatures (Figure S17, Supporting Information). Most interestingly we observed on front side excitation at low temperatures an unusual, delayed signal rise on a µs timescale only for the CsMAFA-st (Figure S17d, Supporting Information), while for the CsMAFA no delayed rise is visible. Such delayed growth implies that photogenerated carriers diffuse toward a

Table 1. Rate constants, trap densities, and mobilities extracted from the fits to TRMC traces of CsMAFA at different temperatures.

T [K] CsMAFA	298	280	260	240	200	160	120
k_2 ($\times 10^{-9}$ cm³s⁻¹)	5.5	6	6	5	5	5	5
k_T ($\times 10^{-9}$ cm³s⁻¹)	4	4	4	4	4	4	4
k_D ($\times 10^{-10}$ cm³s⁻¹)	6	6	6	3	1	1	1
N_T ($\times 10^{14}$ cm⁻³)	0.6	0.55	0.5	0.32	0.1	2	6
p_0 ($\times 10^{13}$ cm⁻³)	0.6	0.55	0.5	0.32	0.1	10	10
k_s ($\times 10^7$ s⁻¹)	0	0	0	0.005	0.03	5.5	10
k_s' ($\times 10^7$ s⁻¹)	0	0	0	0.005	0.03	2	2.5
μ_e (cm² V⁻¹ s⁻¹)	32	34	36	35	33	35	27
μ_h (cm² V⁻¹ s⁻¹)	32	34	36	35	33	35	27

**ADVANCED
SCIENCE NEWS**

www.advancedsciencenews.com

**ADVANCED
FUNCTIONAL
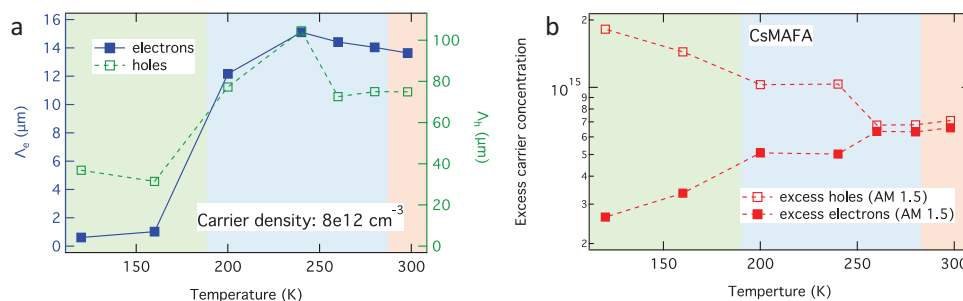MATERIALS**

www.afm-journal.de

Figure 5. a) Charge carrier diffusion length of electrons (left axis, blue) and holes (right axis, green). b) Excess carrier concentration of holes (open squares) and electrons (closed squares) as a function of temperature for the CsMAFA layer.

region in which the carriers obtain higher mobility or the number of shallow traps is less. Therefore we expect that at low temperatures, the CsMAFA-st layer is non-homogeneous. Hence, we did not analyze the XRD pattern in more detail. To verify this asymmetric nature, we performed TRMC measurements using front and back-side excitation at 298 (**Figure 6**a,b) and 130 K (Figure 6c,d) for both layers (See Figure S18 (Supporting Information) for TRMC traces recorded at various intensities and Figure S19 (Supporting Information) for non-normalized TRMC traces of CsMAFA-st on front and back excitations at 298 and 130 K). At 298 K, the front- and back-side TRMC traces do not reveal appreciable differences in the charge carrier dynamics, indicating negligible differences in the top and bottom regions, that is, the entire perovskite layer is homogeneous in the α-phase. The slight difference found using back illumination in comparison to the front side for the CsMAFA is most likely attributed to the presence of some PbI$_2$ at the bottom layer, as discussed in Figure 1a. In addition, in Figure S19 (Supporting Information), a slight increase in signal height using back excitation is observed, which is due to the anti-reflection effect of the quartz substrate.

On comparing Figure 6c,d recorded at 130 K, the TRMC traces observed on the front and back side excitation of the CsMAFA-st layer are substantially different, while for the CsMAFA layer, they are much more comparable. Based on optical spectra (Figure S5, Supporting Information) and free carrier yield calculations (Figure S7, Supporting Information), excitons do not appear to play a role in CsMAFA-st at 130 K. Hence it is suggested that the CsMAFA-st layer is not completely converted to the γ-phase at 130 K. Given the more than two orders of magnitude difference in thermal expansion coefficient between quartz ($\alpha_v = 0.54 \times 10^{-6}$ K^{-1}) and MHPs ($\alpha_v \approx 100-400 \times 10^{-6}$ K^{-1}),[37,66–68] some phase retention in the CsMAFA-st layer might occur as described previously for other MHPs.[69] This implies that on cooling to 130 K, the top part of the CsMAFA-st perovskite layer has converted to γ-phase, but the bottom part close to the quartz substrate is still in the β-phase (See Figure 6e). Hence on front excitation of CsMAFA-st, the generated carriers in the top part can diffuse from the γ-phase to the bottom region which is in the β-phase. Since the diffusion of electrons is in competition with the shallow trapping process in the γ-phase, the resulting rise in signal growth occurs very slowly, that is, within a few μs. However, after this period the excess carriers have obtained an on average higher mobility.

To further verify the asymmetric nature within the entire layer, we recorded the photoconductance traces using front-side excita-

tion wavelengths of 650, 550, and 450 nm, respectively (Figure S20, Supporting Information). Since the penetration depth at 450 nm is less than that at 650 nm, we are able to selectively excite the top part, meaning the initially generated free carriers are more distant from the β-phase. Figure S20b (Supporting Information) shows indeed that the shorter the excitation wavelengths, the slower the delayed signal of TRMC traces. Instead, the excitation-dependent TRMC traces at 298 K are nicely overlapping (Figure S20a, Supporting Information). Furthermore, the normalized TRMC traces from back excitation nearly overlap, independent of excitation wavelength (See Figure S20c, Supporting Information). Combining these observations, we can rule out that excitons have a decisive influence on the TRMC decay. This indeed confirms our hypothesis that the delayed rise in TRMC signal in the CsMAFA-st layer originates from charge carriers diffusing from the top part residing in the γ-phase to the bottom part which is still in the β-phase. For the CsMAFA layer, showing no delayed rise and little difference between front and back excitation, the layer is completely converted into the γ-phase at 130 K. The absence of substantial phase retention is probably due to the presence of excess PbI$_2$ ($\alpha_v = 40 \times 10^{-6}$ K^{-1}) residing between the substrate and CsMAFA layer as concluded from the GIXRD measurement. We anticipate that the excess PbI$_2$ at the interface detaches the CsMAFA layer from the quartz. Moreover, the enlarged crystal domain size in CsMAFA may also facilitate the phase transition as some of the crystal domains go through the entire layer (See the cross-section SEM images in Figure S21, Supporting Information).

Now we get back to the original question of how temperature-induced structural changes affect the optoelectronic properties of the CsMAFA layer. As mentioned no abrupt changes in structural or optical properties are visible, which means that the phase transitions are gradual processes. As argued previously,[70] this might be due to the fact that for FA-rich MHPs the driving force for a phase transition is rather small. Effects of grain sizes or substrates can accelerate or retard the phase transition.[69,71]

Next, it is of interest to evaluate which type of defects is responsible for the observed charge carrier dynamics (band structures for the different phases are provided in Scheme 2). On lowering the temperature from 298 to 200 K we find lower concentrations of deep defects. We speculate that this reduction in deep defects in the β-phase is likely linked to the drop in tensile microstrain since we observe the smallest microstrain at around 240 K. Furthermore, in the γ-phase we find that both the number of deep and shallow states increases substantially. Considering the latter,

**ADVANCED
SCIENCE NEWS**

www.advancedsciencenews.com

**ADVANCED
FUNCTIONAL
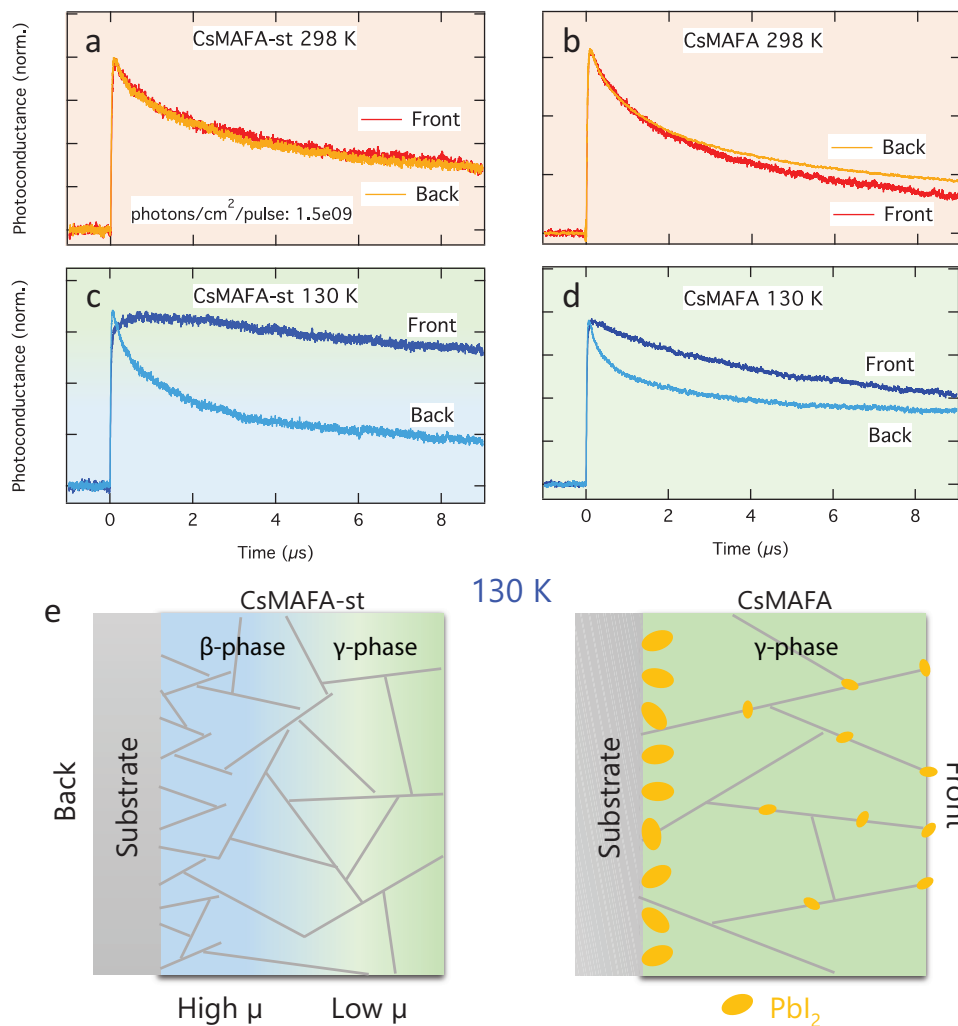MATERIALS**

www.afm-journal.de

Figure 6. Normalized TRMC traces for a,c) CsMAFA-st, b,d) CsMAFA layers recorded at (a,b) 298 and c,d) 130 K on excitation at 650 nm for the front and back excitation at an incident intensity of around 2×10^9 photons cm^{-2} per pulse. e) An illustration of the proposed structural phase transition at 130 K in the CsMAFA-st (left) and CsMAFA (right) layers deposited on the quartz substrate, respectively. The blue shade represents the β-phase, and the green shade the γ-phase. The yellow dots are denoted as excess PbI$_2$. In addition, the grey lines indicate the crystal domain size from the cross-section view.

it has been reported that the FA$_i$ interstitial and V$_I$ vacancy form point defects close to the CBM in FAPbI$_3$ MHPs.[72–74] Hence we anticipate that although these point defects are harmless at 298 K as they are located above/close to the CBM, on cooling they become harmful since the thermal energy ($k_B T$) reduces or the energy difference between CBM and shallow defect level increases. This implies that in the γ-phase most of the time electrons are immobilized in the shallow states and the dominant contribution to the photoconductance is from the mobile holes, leading to the long tails in TRMC signals (Figure 4d).

Finally, from the TRMC measurements, we conclude that the concentration of deep defects also increases substantially in the γ-phase. However, at these low temperatures, spontaneous defect formation becomes less likely. Yet, from the analysis of the XRD patterns a steep rise in microstrain is observed, which might be related to the increased concentration of defects in the γ-phase. On cooling stacking faults or edge dislocations previously observed by atomic-resolution scanning transmission electron microscopy (TEM)[75] might be formed in the γ-phase. Such types of defects can be expected to be fully reversible in line with the reversible structural and optoelectronic changes observed. Future research into cryogenic atomic-resolution scanning TEM may help to learn more about the nature of shallow and deep defects, combined with DFT calculations to gain insight into the corresponding defect levels.

To find out to what extent the observed optoelectronic properties of CsMAFA and CsMAFA-st are applicable to other FA-rich MHPs, we prepared CsMAFA lacking 5% of PbI$_2$ (CsMAFA-shortage) and CsMAFA treated with phenethylammonium iodide (CsMAFA+PEAI). Using temperature-dependent TRMC as shown in Figure S22 (Supporting Information) the charge carrier decay dynamics for CsMAFA+PEAI are very similar to those we observed in CsMAFA without post-treatment. More specifically at 110 K, most of the TRMC traces overlap at low incident light

**ADVANCED
SCIENCE NEWS**

www.advancedsciencenews.com

**ADVANCED
FUNCTIONAL
MATERIALS**

www.afm-journal.de

intensities implying that the concentration of deep defects is again relatively large in the γ-phase, which implies that indeed defects in the bulk are responsible for the observed behavior. In contrast, the decay kinetics in CsMAFA-shortage exhibit a behavior close to that of the stoichiometric CsMAFA-st, with the delayed signal rise at 130 K. From the fact that there is no excess PbI_2 at the interface between quartz and CsMAFA-shortage (Figure S23, Supporting Information) we can expect phase retention near the quartz substrate leading to a non-homogeneous sample giving rise to the delayed ingrowth. Hence, we can conclude that the observed variations in optoelectronic properties coupled with the amount of PbI_2 are quite common in FA-rich MHPs. Moreover, for both types of samples, the effect of shallow states is according to our measurements at room temperature very limited, while the concentration of deep defects shows a minimum at around 200 K.

3. Conclusions

In this work, the structural and optoelectronic properties of Cs-MAFA in different crystal phases were investigated by XRD, optical, and TRMC measurements. First, CsMAFA undergoes an α–β phase transition between 298 and 270 K and a further phase transition to the γ-phase at around 180 K. It is found the E_g monotonically reduces without discontinuities across the range of 298 and 100 K. Moreover, as temperature decreases, the effective carrier mobility is enhanced in the β phase, which is attributed to a reduction of phonon scattering, since the effective masses of both carriers, as shown by DFT calculations, remain very comparable. From the photoconductance measurements, we conclude that CsMAFA exhibits the longest charge carrier diffusion lengths with the lowest deep trap densities close to 240 K, in line with the highest efficiency reported for CsMAFA-based devices at 220 K. Since the microstrain in CsMAFA amounts close to 0 at this temperature, we expect that this plays an essential role in the formation of deep defects in FA-rich perovskites.

On conversion from the β to the γ-phase shallow defects close to the CB become detrimental to the charge carrier dynamics in MHPs. Although these point defects are harmless at 298 K as they are located above/close to the CBM, on cooling they become harmful since the thermal energy reduces or the energy difference between CBM and shallow defect level increases. Hence in the γ-phase most of the time electrons are immobilized in the shallow states. Apart from the shallow states the magnitude of deep traps in the γ-phase increases by an order of magnitude, which is most likely directly correlated with the enhancement in compressive microstrain. The presence of both shallow and deep defects leads to a huge unbalance between electron and hole diffusion lengths.

In contrast to CsMAFA containing a small excess of PbI_2, stoichiometric CsMAFA-st suffers from phase retention of the CsMAFA close to the substrate, which yields an inhomogeneous layer at 130 K comprising a γ-phase on top and a β-phase near the quartz surface. Carriers formed in the top slowly diffuse toward the bottom leading to a remarkable delayed rise in the photoconductance measurements. For the sample with excess PbI_2, it is expected that the PbI_2 residing at the interface detaches the CsMAFA from the quartz substrate leading to a homogeneous layer. Our work provides valuable insight into the temperature-dependent interplay between the structure and the charge carrier dynamics in CsMAFA. Basically, it shows that for FA-rich samples, the β-phase seems the most optimal phase from both structural and optoelectronic points of view.

4. Experimental Section

Preparation of CsMAFA Perovskite Layers: Quartz substrates were rinsed with acetone and ethanol in an ultrasonic bath for 10 min each. Subsequently, an oxygen plasma treatment was performed prior to layer deposition. To prepare the CsMAFA precursor solution, PbI_2 (1.6 mmol, 735.3 mg), FAI (1.31 mmol, 224.4 mg), MABr (0.15 mmol, 16.2 mg), and CsI (0.08 mmol, 19.8 mg) were dissolved in 1 mL of a mixed organic solvent system comprising anhydrous DMF and anhydrous DMSO at a volume ratio of DMF:DMSO of 4:1. For the excess PbI_2 CsMAFA, 5% excess PbI_2 was added to the precursor solution.[30] A stoichiometric ratio of the precursors was prepared for the control sample denoted with CsMAFA-st. The precursor solution was stirred overnight under ≈70 °C. The perovskite layer was deposited using an antisolvent method. A volume of 80 µL of the precursor solution was deposited evenly onto the quartz substrate, and a two-step spin-coating method was applied in a nitrogen-filled glovebox. The first step was carried out at 2000 r.p.m. with an acceleration rate of 200 r.p.m. s^{-1} for 10 s. The second step was at 6000 r.p.m. with an acceleration rate of 2000 r.p.m. s^{-1} for 30 s. As antisolvent 150 µL of diethyl ether was introduced 5 s before the end of the second step. The films were annealed at 120 °C for 15 min. The thickness of the perovskite layer was about 500 nm measured by the profiler meter and the cross-section SEM image.

Structural Characterization: XRD at room temperature was performed on a Bruker D8 ADVANCE diffractometer in Bragg–Brentano configuration using Cu-Kα (λ = 1.54 Å) radiation.

The low-temperature XRD data were recorded on the Panalytical X'pert Pro Diffractometer in Bragg–Brentano mode with a Cu-Kα anode at 45 kV, 40 mA, 1D X'Celerator detector, 0.04 Rad Soller slit, 1/2° fixed exit and divergence slit. The sample was positioned inside the Anton Paar TTK 450 with Kapton windows, an Anton Paar TCU 100 temperature control unit, and a motorized controlled height stage that automatically corrects the height for the thermal expansion and measured under vacuum ($P < 7 \times 10^{-2}$ mbar). Cooling was performed with liquid N_2 and at each temperature the authors waited 15 min after reaching the temperature to ensure the sample was in thermal equilibrium.

Grazing-incidence XRD was conducted on a Bruker D8 DISCOVER diffractometer (Cu-Kα) in combination with an Anton Paar XRK 900 Reactor chamber equipped with Be windows. The measurements were performed in Bragg–Brentano configuration under vacuum (10^{-4} mbar) with variable incident angles of 0.2°, 0.5°, 1°, 3°, and 5° to tune the probed depth. On the primary side, a Goebel mirror was used together with a fixed slit of 0.1, 0.1, 0.2, 0.6, and 1.0 mm, respectively, for the incident angles to control the footprint on the film. On the secondary side, a Soller 2.5° slit was used, and the LYNXEYE XE detector was operated in 0D high-resolution mode.

Structure modeling was performed on the basis of the low-temperature XRD data. PROFEX 5.1[31] was used for both La Bail and Rietveld refinement with a pseudo-Voigt profile function. La Bail method allows us to refine peak positions and intensities without a structure model. PROFEX 5.1 involves an instrument profile that matches this XRD configuration to correct for the broadening of the diffractometer and the background. The primary structural models used in the refinement were based on the space group Pm-3m (no.221) and P4/mbm (no.127) at 298 K, and the space group P4/mbm (no.127) at 270–100 K. Pure FAPbI3 was assumed to suffice since CsMAFA contains only a small amount (3%) of Br and the contribution of organic cations to the XRD pattern was minimal. For the cubic phase, the FA position was fixed at C (0.5, 0.5, 0.5) and N (0.275, 0.5, 0.5) with C—N = 1.43 Å. The occupancies of C and N match with the actual situation, only the peak shape and U_{iso} of Pb and I were refined. For the refinement of the tetragonal phase, the same strategy was applied. In

addition to the fixed FA position, two independent I positions I1(0, 0, 0) and I2(x, 0.5 + x, 0.5) were refined.

Before applying the Williamson–Hall plot analysis, XRD patterns were stripped from the Kα_2 contribution at all temperatures using the DIFFRAC.EVA software from Brucker AXS. The diffraction peaks were fitted with the Voigt function to obtain peak widths.

The surface and cross-section morphologies of perovskite films were characterized using SEM (FESEM; JEJOL JSM-7600F) under an accelerating voltage of 5 and 1 keV, respectively. The perovskites were deposited on quartz substrates.

Optical Characterization: Absorption spectra were recorded with a PerkinElmer Lambda 1050 spectrophotometer equipped with an integrated sphere. The samples were placed inside the sphere to measure the total fraction of reflected and transmitted light (F_{R+T}). Then the fraction of absorbed light (F_A) was calculated by

$$F_A = 1 - F_{R+T} \tag{2}$$

Temperature-dependent steady-state absorption and emission spectra were measured in a home-built He-cryostat spectroscopy setup. The sample was placed in a vacuum chamber (10^{-7} mbar) of which the temperature was controlled using an APD-cryogenics helium cryostat in the range 293–60 K. The optical absorption spectra were recorded using the halogen lamp output of a DH-200 Mikropack UV–vis–NIR light source and a Maya2000 Pro Ocean Optics spectrometer detector. The fluorescence emission spectra were measured using a 405 nm laser pulse of a CPS405 ThorLabs laser diode and a FLAME-S–vis–NIR Ocean Optics spectrometer. At each temperature, the authors waited 15 min after reaching the temperature to ensure the sample was in thermal equilibrium.

Photoconductance Measurement: The TRMC technique was performed to investigate the photoconductance as a function of time using an excitation wavelength in a range of 450–600 nm for CsMAFA. With this technique, the reduction in microwave power ($\Delta P(t)/P$) induced by a laser pulse (repetition rate 10 Hz) was related to the change in conductance ($\Delta G(t)$) by the sensitivity factor K

$$\frac{\Delta P(t)}{P} = -K \Delta G(t) \tag{3}$$

The TRMC signal was expressed in the product of mobility ($\mu_e + \mu_h$) and charge carrier yield φ, which was calculated from the maximum change in photoconductance ΔG_{max}

$$\varphi(\mu_e + \mu_h) = \frac{\Delta G_{max}}{F_A I_0 e \beta} \tag{4}$$

where F_A is the fraction of light absorbed by the sample at a certain excitation wavelength, I_0 is the laser intensity in number of photons per unit area per pulse, e is the elementary charge, and β is the ratio of the inner dimensions of the microwave cell. The samples were placed in a sealed microwave cell inside the glovebox to ensure that they were not exposed to ambient conditions at any time. For the low-temperature TRMC measurements, liquid N_2 was used to cool down samples. After reaching a specific temperature a waiting period of 15 min was used to ensure the sample was in thermal equilibrium.

Supporting Information

Supporting Information is available from the Wiley Online Library or from the author.

Acknowledgements

Conflict of Interest

The authors declare no conflict of interest.

Data Availability Statement

The data that support the findings of this study are available from the corresponding author upon reasonable request.

Keywords

[1] M. Grätzel, *Nat. Mater.* **2014**, *13*, 838.

[2] S. D. Stranks, G. E. Eperon, G. Grancini, C. Menelaou, M. J. P. Alcocer, T. Leijtens, L. M. Herz, A. Petrozza, H. J. Snaith, *Science* **2013**, *342*, 341.

[3] H. Tan, A. Jain, O. Voznyy, X. Lan, F. P. García De Arquer, J. Z. Fan, R. Quintero-Bermudez, M. Yuan, B. Zhang, Y. Zhao, F. Fan, P. Li, L. N. Quan, Y. Zhao, Z.-H. Lu, Z. Yang, S. Hoogland, E. H. Sargent, *Science* **2017**, *355*, 722.

[4] E. M. Tennyson, T. A. S. Doherty, S. D. Stranks, *Nat. Rev. Mater.* **2019**, *4*, 573.

[5] N.-G. Park, K. Zhu, *Nat. Rev. Mater.* **2020**, *5*, 333.

[6] Y. He, M. Petryk, Z. Liu, D. G. Chica, I. Hadar, C. Leak, W. Ke, I. Spanopoulos, W. Lin, D. Y. Chung, B. W. Wessels, Z. He, M. G. Kanatzidis, *Nat. Photonics* **2021**, *15*, 36.

[7] A. Fakharuddin, M. K. Gangishetty, M. Abdi-Jalebi, S.-H. Chin, A. R. Bin Mohd Yusoff, D. N. Congreve, W. Tress, F. Deschler, M. Vasilopoulou, H. J. Bolink, *Nat. Electron.* **2022**, *5*, 203.

[8] NREL, Best Research-Cell Efficiencies, https://www.nrel.gov/pv/cell-efficiency.html (accessed: September 2023).

[9] L. Liu, A. Mei, X. Li, H. Han, Y. Dkhissi, A. D. Scully, R. A. Caruso, Y. B. Cheng, I. Jeong, J. Lee, M. J. Ko, K. Yong, B. S. Richards, T. L. Kelly, N. Pellet, M. Levi, S. Turri, M. Levi, S. Turri, *Science* **2016**, *354*, 206.

[10] T. Bu, J. Li, F. Zheng, W. Chen, X. Wen, Z. Ku, Y. Peng, J. Zhong, Y.-B. Cheng, F. Huang, *Nat. Commun.* **2018**, *9*, 4609.

[11] Y. Zhao, H. Tan, H. Yuan, Z. Yang, J. Z. Fan, J. Kim, O. Voznyy, X. Gong, L. N. Quan, C. S. Tan, J. Hofkens, D. Yu, Q. Zhao, E. H. Sargent, *Nat. Commun.* **2018**, *9*, 6071.

[12] M. M. Tavakoli, M. Saliba, P. Yadav, P. Holzhey, A. Hagfeldt, S. M. Zakeeruddin, M. Grätzel, *Adv. Energy Mater.* **2019**, *9*, 8026461.

[13] S. Wang, J. Jin, Y. Qi, P. Liu, Y. Xia, Y. Jiang, R. X. He, B. Chen, Y. Liu, X. Z. Zhao, *Adv. Funct. Mater.* **2020**, *30*, 1908343.

[14] X. Zheng, Y. Hou, C. Bao, J. Yin, F. Yuan, Z. Huang, K. Song, J. Liu, J. Troughton, N. Gasparini, C. Zhou, Y. Lin, D.-J. Xue, B. Chen, A. K. Johnston, N. Wei, M. N. Hedhili, M. Wei, A. Y. Alsalloum, P. Maity, B. Turedi, C. Yang, D. Baran, T. D. Anthopoulos, Y. Han, Z.-H. Lu, O. F. Mohammed, F. Gao, E. H. Sargent, O. M. Bakr, *Nat. Energy* **2020**, *5*, 131.

**ADVANCED
SCIENCE NEWS**

www.advancedsciencenews.com

**ADVANCED
FUNCTIONAL
MATERIALS**

www.afm-journal.de

[15] T. Li, S. Wang, J. Yang, X. Pu, B. Gao, Z. He, Q. Cao, J. Han, X. Li, *Nano Energy* **2021**, *82*, 105742.

[16] S. You, H. Zeng, Y. Liu, B. Han, M. Li, L. Li, X. Zheng, R. Guo, L. Luo, Z. Li, C. Zhang, R. Liu, Y. Zhao, S. Zhang, Q. Peng, T. Wang, Q. Chen, F. T. Eickemeyer, B. Carlsen, S. M. Zakeeruddin, L. Mai, Y. Rong, M. Grätzel, X. Li, *Science* **2023**, *379*, 288.

[17] M. Saliba, T. Matsui, J. Y. Seo, K. Domanski, J. P. Correa-Baena, M. K. Nazeeruddin, S. M. Zakeeruddin, W. Tress, A. Abate, A. Hagfeldt, M. Grätzel, *Energy Environ. Sci.* **2016**, *9*, 1989.

[18] A. S. R. Bati, Y. L. Zhong, P. L. Burn, M. K. Nazeeruddin, P. E. Shaw, M. Batmunkh, *Commun. Mater.* **2023**, *4*, 2.

[19] Y. Chen, S. Tan, N. Li, B. Huang, X. Niu, L. Li, M. Sun, Y. Zhang, X. Zhang, C. Zhu, N. Yang, H. Zai, Y. Wu, S. Ma, Y. Bai, Q. Chen, F. Xiao, K. Sun, H. Zhou, *Joule* **2020**, *4*, 1961.

[20] H. Afshari, B. K. Durant, A. R. Kirmani, S. A. Chacon, J. Mahoney, V. R. Whiteside, R. A. Scheidt, M. C. Beard, J. M. Luther, I. R. Sellers, *ACS Appl. Mater. Interfaces* **2022**, *14*, 44358.

[21] R. L. Milot, G. E. Eperon, H. J. Snaith, M. B. Johnston, L. M. Herz, *Adv. Funct. Mater.* **2015**, *25*, 6218.

[22] C. Greenland, A. Shnier, S. K. Rajendran, J. A. Smith, O. S. Game, D. Wamwangi, G. A. Turnbull, I. D. W. Samuel, D. G. Billing, D. G. Lidzey, *Adv. Energy Mater.* **2020**, *10*, 901350.

[23] G. W. Kim, A. Petrozza, *Adv. Energy Mater.* **2020**, *10*, 2001959.

[24] T. J. Jacobsson, J.-P. Correa-Baena, E. H. Anaraki, B. Philippe, S. D. Stranks, M. E. F. Bouduban, W. Tress, K. Schenk, J. Teuscher, J.-E. Moser, H. Rensmo, A. Hagfeldt, *J. Am. Chem. Soc.* **2016**, *138*, 10331.

[25] T. Meier, T. P. Gujar, A. Schönleber, S. Olthof, K. Meerholz, S. Van Smaalen, F. Panzer, M. Thelakkat, A. Köhler, *J. Mater. Chem. C* **2018**, *6*, 7512.

[26] A. Merdasa, A. Kiligaridis, C. Rehermann, M. Abdi-Jalebi, J. Stöber, B. Louis, M. Gerhard, S. D. Stranks, E. L. Unger, I. G. Scheblykin, *ACS Energy Lett.* **2019**, *4*, 1370.

[27] J. Euvrard, O. Gunawan, D. B. Mitzi, *Adv. Energy Mater.* **2019**, *9*, 1902706.

[28] B. Roose, K. Dey, Y.-H. Chiang, R. H. Friend, S. D. Stranks, *J. Phys. Chem. Lett.* **2020**, *11*, 6505.

[29] Y. Gao, H. Raza, Z. Zhang, W. Chen, Z. Liu, *Adv. Funct. Mater.* **2023**,, 221517.

[30] H. Zhu, Z. Shen, L. Pan, J. Han, F. T. Eickemeyer, Y. Ren, X. Li, S. Wang, H. Liu, X. Dong, S. M. Zakeeruddin, A. Hagfeldt, Y. Liu, M. Grätzel, *ACS Energy Lett.* **2021**, *6*, 208.

[31] N. Doebelin, R. Kleeberg, *J. Appl. Crystallogr.* **2015**, *48*, 1573.

[32] Y. Vaynzof, *Adv. Energy Mater.* **2020**, *10*, 2003073.

[33] A. D. Taylor, Q. Sun, K. P. Goetz, Q. An, T. Schramm, Y. Hofstetter, M. Litterst, F. Paulus, Y. Vaynzof, *Nat. Commun.* **2021**, *12*, 1878.

[34] L. Chen, Y.-Y. Tan, Z.-X. Chen, T. Wang, S. Hu, Z.-A. Nan, L.-Q. Xie, Y. Hui, J.-X. Huang, C. Zhan, S.-H. Wang, J.-Z. Zhou, J.-W. Yan, B.-W. Mao, Z.-Q. Tian, *J. Am. Chem. Soc.* **2019**, *141*, 1665.

[35] Z. Li, B. Li, X. Wu, S. A. Sheppard, S. Zhang, D. Gao, N. J. Long, Z. Zhu, *Science* **2022**, *376*, 416.

[36] C. C. Stoumpos, C. D. Malliakas, M. G. Kanatzidis, *Inorg. Chem.* **2013**, *52*, 9019.

[37] D. H. Fabini, C. C. Stoumpos, G. Laurita, A. Kaltzoglou, A. G. Kontos, P. Falaras, M. G. Kanatzidis, R. Seshadri, *Angew. Chem.* **2016**, *128*, 15618.

[38] O. J. Weber, D. Ghosh, S. Gaines, P. F. Henry, A. B. Walker, M. S. Islam, M. T. Weller, *Chem. Mater.* **2018**, *30*, 3768.

[39] S. Kawachi, M. Atsumi, N. Saito, N. Ohashi, Y. Murakami, J.-I. Yamaura, *J. Phys. Chem. Lett.* **2019**, *10*, 6967.

[40] M. Keshavarz, M. Ottesen, S. Wiedmann, M. Wharmby, R. Küchler, H. Yuan, E. Debroye, J. A. Steele, J. Martens, N. E. Hussey, M. Bremholm, M. B. J. Roeffaers, J. Hofkens, *Adv. Mater.* **2019**, *31*, 1900521.

[41] E. G. Moloney, V. Yeddu, M. I. Saidaminov, *ACS Mater. Lett.* **2020**, *2*, 1495.

[42] G. F. Harrington, J. Santiso, *J. Electroceramics* **2021**, *47*, 141.

[43] C. Greenland, A. Shnier, S. K. Rajendran, J. A. Smith, O. S. Game, D. Wamwangi, G. A. Turnbull, I. D. W. Samuel, D. G. Billing, D. G. Lidzey, *Adv. Energy Mater.* **2020**, *10*, 901350.

[44] F. Ruf, M. F. Aygüler, N. Giesbrecht, B. Rendenbach, A. Magin, P. Docampo, H. Kalt, M. Hetterich, *APL Mater.* **2019**, *7*, 031113.

[45] A. D. Wright, C. Verdi, R. L. Milot, G. E. Eperon, M. A. Pérez-Osorio, H. J. Snaith, F. Giustino, M. B. Johnston, L. M. Herz, *Nat. Commun.* **2016**, *7*, 11755.

[46] Y. P. Varshni, *Physica* **1967**, *34*, 149.

[47] M. Ledinsky, T. Schönfeldová, J. Holovský, E. Aydin, Z. Hájková, L. Landová, N. Neyková, A. Fejfar, S. De Wolf, *J. Phys. Chem. Lett.* **2019**, *10*, 1368.

[48] B. J. Foley, D. L. Marlowe, K. Sun, W. A. Saidi, L. Scudiero, M. C. Gupta, J. J. Choi, *Appl. Phys. Lett.* **2015**,*106*, 243904.

[49] M. I. Dar, G. Jacopin, S. Meloni, A. Mattoni, N. Arora, A. Boziki, S. M. Zakeeruddin, U. Rothlisberger, M. Grätzel, *Sci. Adv.* **2016**, *2*, 1601156.

[50] E. M. Hutter, R. J. Sutton, S. Chandrashekar, M. Abdi-Jalebi, S. D. Stranks, H. J. Snaith, T. J. Savenije, *ACS Energy Lett.* **2017**, *2*, 1901.

[51] D. Guo, Z. A. Garmaroudi, M. Abdi-Jalebi, S. D. Stranks, T. J. Savenije, *ACS Energy Lett.* **2019**, *4*, 2360.

[52] J. Zhao, V. M. Caselli, M. Bus, B. Boshuizen, T. J. Savenije, *ACS Appl. Mater. Interfaces* **2021**, *13*, 16309.

[53] T. J. Savenije, D. Guo, V. M. Caselli, E. M. Hutter, *Adv. Energy Mater.* **2020**, *10*, 1903788.

[54] K. Galkowski, A. Mitioglu, A. Miyata, P. Plochocka, O. Portugall, G. E. Eperon, J. T.-W. Wang, T. Stergiopoulos, S. D. Stranks, H. J. Snaith, R. J. Nicholas, *Energy Environ. Sci.* **2016**, *9*, 962.

[55] C. L. Davies, J. Borchert, C. Q. Xia, R. L. Milot, H. Kraus, M. B. Johnston, L. M. Herz, *J. Phys. Chem. Lett.* **2018**, *9*, 4502.

[56] P. Umari, E. Mosconi, F. De Angelis, *J. Phys. Chem. Lett.* **2018**, *9*, 620.

[57] M. Baranowski, P. Plochocka, *Adv. Energy Mater.* **2020**, *10*, 1903659.

[58] V. D'innocenzo, G. Grancini, M. J. P. Alcocer, A. R. S. Kandada, S. D. Stranks, M. M. Lee, G. Lanzani, H. J. Snaith, A. Petrozza, *Nat. Commun.* **2014**, *5*, 3586.

[59] C. L. Davies, M. R. Filip, J. B. Patel, T. W. Crothers, C. Verdi, A. D. Wright, R. L. Milot, F. Giustino, M. B. Johnston, L. M. Herz, *Nat. Commun.* **2018**, *9*, 293.

[60] V. M. Caselli, T. J. Savenije, *J. Phys. Chem. Lett.* **2022**, *13*, 7523.

[61] K. Momma, F. Izumi, *J. Appl. Crystallogr.* **2011**, *44*, 1272.

[62] O. G. Reid, M. Yang, N. Kopidakis, K. Zhu, G. Rumbles, *ACS Energy Lett.* **2016**, *1*, 561.

[63] Q. Chen, H. Zhou, T.-B. Song, S. Luo, Z. Hong, H.-S. Duan, L. Dou, Y. Liu, Y. Yang, *Nano Lett.* **2014**, *14*, 4158.

[64] D. Bi, W. Tress, M. I. Dar, P. Gao, J. Luo, C. Renevier, K. Schenk, A. Abate, F. Giordano, J.-P. Correa-Baena, J.-D. Decoppet, S. M. Zakeeruddin, M. K. Nazeeruddin, M. Grätzel, A. Hagfeldt, *Sci. Adv.* **2016**, *2*, 1501170.

[65] Q. Jiang, Z. Chu, P. Wang, X. Yang, H. Liu, Y. Wang, Z. Yin, J. Wu, X. Zhang, J. You, *Adv. Mater.* **2017**, *29*, 17038521.

[66] T. J. Jacobsson, L. J. Schwan, M. Ottosson, A. Hagfeldt, T. Edvinsson, *Inorg. Chem.* **2015**, *54*, 10678.

[67] F. Brivio, J. M. Frost, J. M. Skelton, A. J. Jackson, O. J. Weber, M. T. Weller, A. R. Goñi, A. M. A. Leguy, P. R. F. Barnes, A. Walsh, *Phys. Rev. B: Condens. Matter Mater. Phys.* **2015**, *92*, 144308.

[68] D. J. Xue, Y. Hou, S. C. Liu, M. Wei, B. Chen, Z. Huang, Z. Li, B. Sun, A. H. Proppe, Y. Dong, M. I. Saidaminov, S. O. Kelley, J. S. Hu, E. H. Sargent, *Nat. Commun.* **2020**, *11*, 1514.

[69] A. Osherov, E. M. Hutter, K. Galkowski, R. Brenes, D. K. Maude, R. J. Nicholas, P. Plochocka, V. Bulovic, T. J. Savenije, S. D. Stranks, *Adv. Mater.* **2016**, *28*, 10757.

[70] B. A. Rosales, K. Schutt, J. J. Berry, L. M. Wheeler, *ACS Energy Lett.* **2023**, *8*, 1705.

[71] C. Stavrakas, S. J. Zelewski, K. Frohna, E. P. Booker, K. Galkowski, K. Ji, E. Ruggeri, S. Mackowski, R. Kudrawiec, P. Plochocka, S. D. Stranks, *Adv. Energy Mater.* **2019**, *9*, 1901883.

[72] H. Xue, G. Brocks, S. Tao, *Phys. Rev. Mater.* **2022**, *6*, 055402.

[73] L. Cheng, B. Xu, Y. Zeng, L. Meng, *Phys. Chem. Chem. Phys.* **2023**, *25*, 6369.

[74] N. Liu, C. Yam, *Phys. Chem. Chem. Phys.* **2018**, *20*, 6800.

[75] M. U. Rothmann, J. S. Kim, J. Borchert, K. B. Lohmann, C. M. O'Leary, A. A. Sheader, L. Clark, H. J. Snaith, M. B. Johnston, P. D. Nellist, L. M. Herz, *Science* **2020**, *370*, 548.